Heterogeneous Catalysis

DOI: 10.1002/anie.201005282

# On the Surface Chemistry of Iron Oxides in Reactive Gas Atmospheres**

*Emiel de Smit, Matti M. van Schooneveld, Fabrizio Cinquini, Hendrik Bluhm, Phillippe Sautet, Frank M. F. de Groot,* and Bert M. Weckhuysen**

Heterogeneous catalysis is based on the generation and subsequent combination of chemical species retained on the surface of a catalytic solid. Elementary reaction steps, that is, the dissociation of reactants and association to products, take place at the solid–gas or solid–liquid interface. Therefore, maximizing the accessible specific catalytic surface area, by reducing primary particle sizes, increases the (weight based) catalyst activity and results in higher material efficiency. However, surface and electronic properties of solids are often also significantly altered with decreasing particle sizes.[1,2] This results in size-dependent catalytic performance, better known as the particle size effect.[3–5] Although this effect has been well documented for many catalytic reactions, the exact underlying reasons for the different performance are often more difficult to access.

Here, we report on the surface chemistry of iron oxides of different initial particle size in reactive gas atmospheres as probed by in situ X-ray photoelectron spectroscopy (XPS).[6–9] Although mbar pressures were applied, in situ XPS constitutes an initial step in bridging the so-called pressure gap between surface science (traditionally ultrahigh vacuum) and heterogeneous catalysis (1–200 bar), and provides unique insights into the mutual influence of surface structure and adsorption properties of a solid. Comparison of a nanoparticulate and bulk iron oxide allowed us to probe the size dependence of the iron, oxygen, and carbon surface chemistry in different gas atmospheres, while the general observed transformations in carbon-containing iron phases in both samples were explained by ab initio atomistic thermodynamics.[10–12] The results hold relevance for Fe-based catalysts, in particular Fe-based Fischer–Tropsch synthesis catalysts, which are important in the conversion of coal, biomass, and natural gas to hydrocarbon transportation fuels and chemicals.[13–15]

Nanoparticulate iron oxide, similar to catalyst materials used in industry,[13] was prepared by precipitation. A bulk iron oxide sample was acquired commercially. Section S1 and Figure S1 in the Supporting Information give the detailed preparation method and representative transmission electron microscopy (TEM) images of both samples. The nanoparticulate iron oxide sample consists of agglomerates of small (ca. 5 nm) $\alpha$-$Fe_2O_3$ crystallites, whereas the bulk sample shows $\alpha$-$Fe_2O_3$ crystallites of approximately 100 nm. The Brunauer–Emmett–Teller (BET) surface area of the materials was 136 $m^2 g^{-1}$ for the nanoparticulate iron oxide and 17 $m^2 g^{-1}$ for the bulk iron oxide.

For the XPS experiments, the materials were suspended in isopropyl alcohol and deposited on pre-cleaned diced Si wafers. The deposition was repeated until the wafers were completely covered in sample. Any residual carbonaceous surface species were removed by treatment in 0.3 Torr $O_2$ at 300 °C. The inertness of the Si wafers in the gas atmospheres was evaluated by means of reference experiments on blank Si wafers. Section S2 in the Supporting Information gives a detailed description of the experimental setup, sample preparation, applied excitation energies, energy calibration, and atomic ratio calculations.

Figure 1 shows the Fe 2p and O 1s XPS spectra, and the calculated atomic O/Fe ratios for the two samples during treatment in 0.2 Torr $H_2$. At 275 °C in vacuum, both materials consist of $\alpha$-$Fe_2O_3$, as indicated by the Fe $2p_{3/2}$ peak at 710.5 eV[16] (Figure 1 a,d) and associated shake-up structure. In addition, the O 1s spectra showed the contribution of a single peak at 529.8 eV[17] (Figure 1 b,e), characteristic for O in $\alpha$-$Fe_2O_3$. Upon exposure to $H_2$ and heating to 300 °C, a shoulder appeared in the Fe $2p_{3/2}$ spectrum at 709.8 eV, assigned to $Fe^{2+}$ species in $Fe_3O_4$ and FeO.[16] At the same time, the main peak in the O 1s spectrum shifted to higher binding energy (530.1 eV), characteristic for the lower valence of Fe.[17] In addition, a shoulder appeared in the O

[*] E. de Smit, M. M. van Schooneveld, Prof. Dr. F. M. F. de Groot, Prof. Dr. B. M. Weckhuysen
Inorganic Chemistry and Catalysis
Debye Institute for Nanomaterials Science, Utrecht University
Sorbonnelaan 16, 3584 CA Utrecht (The Netherlands)
Fax: (+31) 30-251-1027
E-mail: f.m.f.degroot@uu.nl
b.m.weckhuysen@uu.nl
Dr. F. Cinquini, Prof. Dr. P. Sautet
Université de Lyon, Institut de Chimie de Lyon, Laboratoire de Chimie, École Normale Supérieure de Lyon and CNRS
46 Allée d'Italie, 69364 Lyon Cedex 07 (France)
Dr. H. Bluhm
Chemical Sciences Division
Ernest Orlando Lawrence Berkeley National Laboratory
1 Cyclotron Road, Berkeley, CA 94720 (USA)

[**] Financial support is acknowledged from Shell Global Solutions (B.M.W.), the Dutch National Science Foundation (CW-NWO/VICI program) (F.M.F.d.G. and B.M.W.), and the Netherlands Research School Combination on Catalysis (NRSC-C) (B.M.W.). This work was performed at the Advanced Light Source (ALS) at the Lawrence Berkeley National Laboratory in Berkeley, USA. The ALS is supported by the Director, Office of Science, Office of Basic Energy Sciences, of the US Department of Energy under Contract No. DE-AC02-05CH11231. P. Miedema and Dr. I. González Jiménez (Utrecht University) are acknowledged for their help in XPS data acquisition.

Supporting information for this article is available on the WWW under http://dx.doi.org/10.1002/anie.201005282.

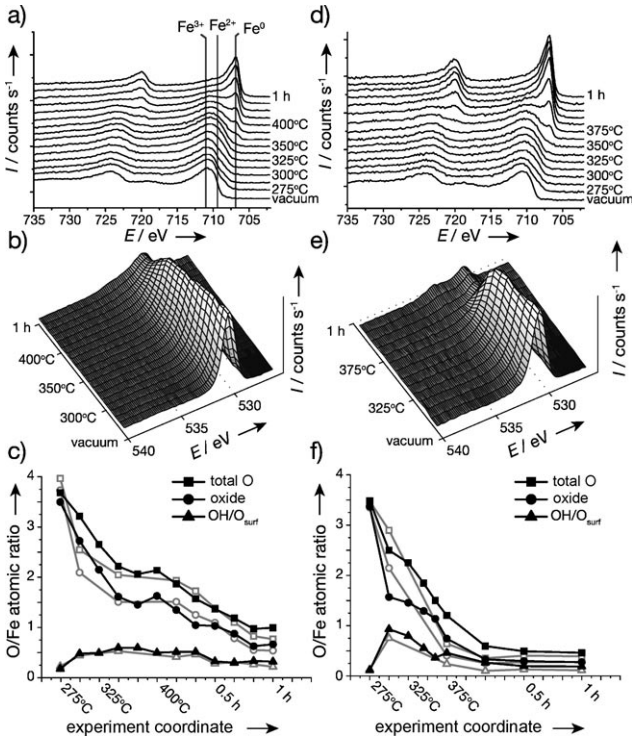


***Figure 1.*** a, d) Fe 2p and b, e) O 1s XPS spectra (both at 200 eV KE, 7 Å IMFP) and c, f) calculated O/Fe atomic ratios of various oxygen-containing species for the nanoparticulate iron oxide (a–c) and bulk iron oxide (d–f) during treatment in $H_2$. The closed black symbols indicate ratios at 200 eV KE (7 Å IMFP), the open gray symbols indicate ratios at 450 eV KE (11 Å IMFP).

1s spectrum at 530.8 eV, assigned to surface oxygen species, probably present as surface OH groups. Both samples showed a significant increase in OH/Fe ratios upon initial exposure to $H_2$ gas. The bulk iron oxide showed a higher OH/Fe ratio up to 350 °C. This is in line with recent observations that bulk α-$Fe_2O_3$ binds water more tightly than nanoparticulate hematite by a factor of 2.[2]

Upon heating to 375 °C, the bulk oxide quickly reduces to metallic Fe, as indicated by the rapid growth of the Fe $2p_{3/2}$ XPS peak at 706.8 eV together with the drop in O/Fe ratios. After 30 min at 375 °C, the sample is completely reduced with a final O/Fe ratio of 0.46 at 7 Å and 0.39 at 11 Å (inelastic mean free path; IMFP). In contrast, the nanoparticulate material reduces very slowly, with similar O/Fe ratios at 7 and 11 Å probing depth during the treatment. The sample had to be heated to 400 °C to reduce further and even after 1 h, the sample showed a higher contribution of O at the surface with a final O/Fe ratio of 1.0 at 7 Å and 0.78 at 11 Å IMFP. This indicates that the reduction of nanoparticulate iron oxide is more dynamic and has an oxide-rich surface after treatment in $H_2$.

The two samples also followed a significantly different reduction pathway. An isosbestic point was observed above 350 °C in the XPS spectra of the nanoparticulate iron oxide. This was not observed in the reduction of the bulk oxide (Figure S2, Supporting Information). The occurrence of the isosbestic point suggests that only two species contribute to the spectrum. Considering the high $Fe^{3+}/Fe^{2+}$ ratio, and the low stability of this phase, it is unlikely that FeO is present. Therefore, above 350 °C the XPS spectra of the nanoparticulate material only consists of $Fe_3O_4$ and $Fe^0$, suggesting that the final reduction step is inhibited. The absence of an isosbectic point in the case of the bulk iron oxide indicates that the reduction of α-$Fe_2O_3$ to $Fe_3O_4$ and $Fe^0$ occurs simultaneously. Overall, complete reduction is more difficult to achieve in the nanoparticulate sample.

After reduction, the materials were exposed to $CO/H_2$ and CO at different temperatures. The samples were initially cooled from 350 °C in a stepwise manner to 150 °C, while exposing them to 0.3 Torr $CO/H_2$ (0.1 Torr CO/0.2 Torr $H_2$). After this, the samples were heated to 350 °C in 0.3 Torr CO using 50 °C increments. Figure 2 shows the O 1s and C 1s XPS spectra during these treatments.

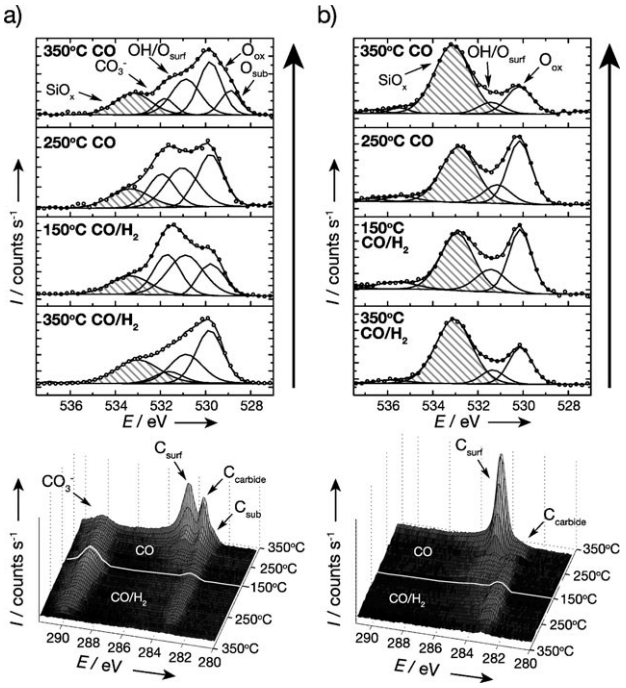


***Figure 2.*** O 1s (top) and C 1s (bottom) XPS spectra of the a) nanoparticulate iron oxide and b) bulk iron oxide during the treatment in 0.3 Torr $CO/H_2$ and 0.3 Torr CO at various temperatures. Hatched areas indicate the possible contribution of the $SiO_x$ wafer. The spectra were acquired at 200 eV KE (ca. 7 Å IMFP).

There are significant differences in the XPS spectra of both samples. At 350 °C in $CO/H_2$, there are little carbon- or oxygen-bearing surface species observed in both materials. Upon cooling to 250 °C, the iron phase in both samples is partially converted into iron carbides, as evidenced by the appearance of a peak at 283.3 eV in the C 1s spectra.[18] The carbide peak is associated with a shoulder at 284.6 eV. The contribution of this shoulder was small, however, and its assignment is not unambiguous. Therefore we will assign it to the occurrence of generic non-oxygenated surface carbon species ($C_{surf}$). In the nanoparticulate material, there is an additional contribution to the C 1s spectrum at 289.8 eV,

  

which is absent in the bulk iron oxide sample. This peak is due to surface carbonate species. The mass spectrometry data measured during the experiment suggested a higher concentration of $CO_2$ during treatment of the nanoparticulate sample (Figure S3, Supporting Information). This might indicate a preferential reduction of the iron oxide by CO in this sample.

The O 1s XPS spectra during $CO/H_2$ treatment show contributions of different oxygen-bearing species. Both samples have a contribution of oxide and surface OH at 530.1 and 530.8 eV, respectively. In addition, both samples show a peak at 533.3 eV. Although this peak can be assigned to adsorbed molecular $H_2O$,[19] the supporting oxygen-terminated $Si/SiO_x$ wafer was partially exposed after $H_2$ treatment, due to shrinkage of the iron oxide layer. The maximum observed Si/Fe ratio was 0.14 at 200 eV kinetic energy (KE). Therefore $SiO_x$ species contribute to the O 1s peak at 533.3 eV, and because of the uncertainty introduced by this, we will not treat the 533.3 eV peak area or $H_2O$ contribution quantitatively. In the O 1s spectrum of the nanoparticulate material, there is an additional contribution at 531.9 eV, further confirming the presence of surface carbonates.[19]

Figure 3 summarizes the evolution of the O/Fe and C/Fe ratios during the different treatments. In both samples, the total coverage of carbon- and oxygen-containing surface

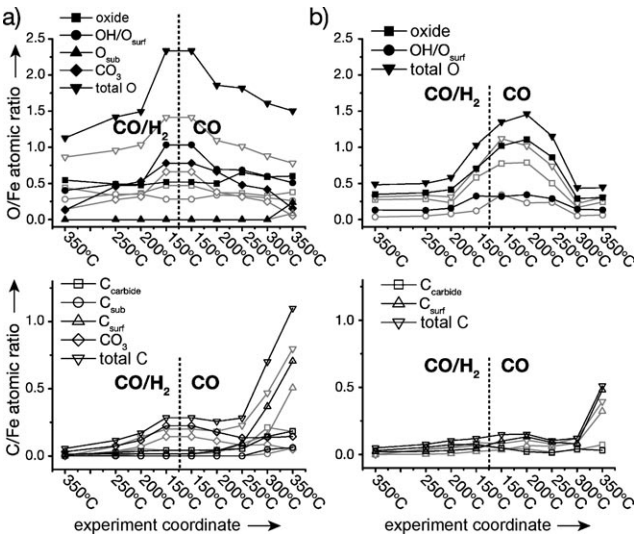


***Figure 3.*** O/Fe and C/Fe ratios for various species during the $CO/H_2$ and CO treatment at various temperatures. a) Nanoparticulate iron oxide and b) bulk iron oxide. Black symbols indicate ratios at 7 Å IMFP, gray symbols indicate ratios at 11 Å IMFP.

species increases at lower temperatures. The iron oxide content in the nanoparticulate material, as derived from the O 1s peak at 530.1 eV, drops during $CO/H_2$ treatment at lower temperatures, while at the same time the coverage of surface OH species and carbonates increases. In contrast, the oxide content of the bulk material increases during $CO/H_2$ treatment, especially at 150 °C. This oxidation is reflected in the Fe 2p XPS spectra acquired during the $CO/H_2$ and CO treatment (Figure S4, Supporting Information). As can be further inferred from Figure 3, the Fe species in nanoparticulate iron oxide remain reduced throughout the experiments. The increase in O/Fe ratios at temperatures below 200 °C is likely to be due to the higher coverage of oxidizing $H_2O$ species that may become adsorbed below this temperature. The contribution of the oxygen-bearing species in both samples is higher at 7 Å compared to 11 Å IMFP, confirming the surface nature of the oxygen-bearing species and excluding the extensive formation of bulk iron oxides.

The C/Fe ratios also increase in both carbon materials during $CO/H_2$ treatment, illustrating that the materials are reactive to CO, even at temperatures as low as 150 °C. The nanoparticulate sample mainly forms carbonates at the surface, whereas a small part of the iron is converted into iron carbides ($C_{carbide}/Fe = 0.04$). The bulk sample shows a larger contribution of carbides ($C_{carbide}/Fe = 0.07$). The ratio between the O 1s and C 1s carbonate peaks was approximately 3, fitting the expected stoichiometry of $CO_3$.

Upon heating the samples in 0.3 Torr CO the bulk material is further oxidized up to 200 °C. Possibly, oxidation in the presence of physisorbed or adsorbed $H_2O$ species competes with the reduction by CO at this temperature. An alternative explanation is the segregation of oxygen from unreduced (bulk) iron oxide, which may be present in deeper layers after reduction in $H_2$, to the surface. The change in gas-phase conditions may induce segregation of oxygen from deeper bulk layers (not observed in XPS) to the surface, apparently oxidizing the surface of the material. At higher temperatures, the contribution of oxide and OH oxygen species decreases gradually. At 300 °C in CO, the O/Fe ratios are back to the ratios found after the $H_2$ treatment.

During the treatment in CO, the contribution of the carbide phase at 7 Å IMFP slowly decreases at the expense of non-oxygenated surface carbon species. Upon reaching 350 °C there is a sharp increase in the C/Fe ratios, primarily due to the buildup of surface carbon species. This buildup is most probably a direct result of the formation of Boudouard coke ($2\,CO \rightarrow CO_2 + C$) on the metallic surface.

The nanoparticulate material shows a different behavior in 0.3 Torr CO. The carbonate species formed during $CO/H_2$ treatment slowly desorb at higher temperatures. The total iron oxide content did not change as drastically as for the bulk material, but remained constant throughout the $CO/H_2$ and CO treatment. It is suggested that the presence of surface carbonates might play a role in protecting the small particles from oxidizing in the presence of $H_2O$. At temperatures above 200 °C, the carbide content of the nanoparticulate material increases up to $C_{carbide}/Fe = 0.2$ for both 7 and 11 Å IMFP, illustrating the formation of bulk iron carbides. Above 250 °C, an increase in surface carbon is observed, probably due to the buildup of Boudouard coke. In this case, however, the contribution of iron carbides increases proportionally with the surface carbon species, showing that the nanoparticulate material is carburized to iron carbides much more facilely and dynamically than the bulk iron oxide. At temperatures above 250 °C, the nanoparticulate sample showed an additional contribution in the C 1s XPS spectra. This contribution at 282.7 eV is assigned to atomically dispersed surface or subsurface carbon, similar to species observed in Pd cata-

  

lysts.[20] At 350 °C, there is also an additional contribution to the O 1s spectrum at 529.0 eV, assigned to subsurface or atomically dispersed adsorbed oxygen species.[6]

The morphology and texture of both samples were analyzed after treatment by $N_2$ physisorption and TEM (Figure S1, Supporting Information). Significant sintering was observed. A carbon layer could be observed on the outer rim of the particles in both samples. The BET surface area of both samples was below 10 $m^2 g^{-1}$ after the experiment.

Figure 4a summarizes the observations of the in situ XPS experiments discussed to this point. Without taking into account the crystallite size dependency, we will now focus on the explanation of the competition between carbon in surface, subsurface, and carbide phases, as observed for both materials, as a function of the applied experimental conditions. For this we have calculated by density functional theory the Gibbs free surface energy $\gamma(T, P)$ of growing surface layers of commonly observed θ-$Fe_3C$ and χ-$Fe_5C_2$ iron carbide phases, and (sub)surface carbon in Fe(110). The chemical potential of carbon atoms, $\mu_C$, as imposed by a gas-phase reservoir at a certain temperature and pressure, is used as a descriptor for the relative stability of surface phases under experimental conditions. This ab initio atomistic thermodynamic approach has been successfully applied to study other systems.[10–12] A detailed description of the theoretical methodology and the structure of the studied surfaces are given in Section S3 and Figure S5 in the Supporting Information.

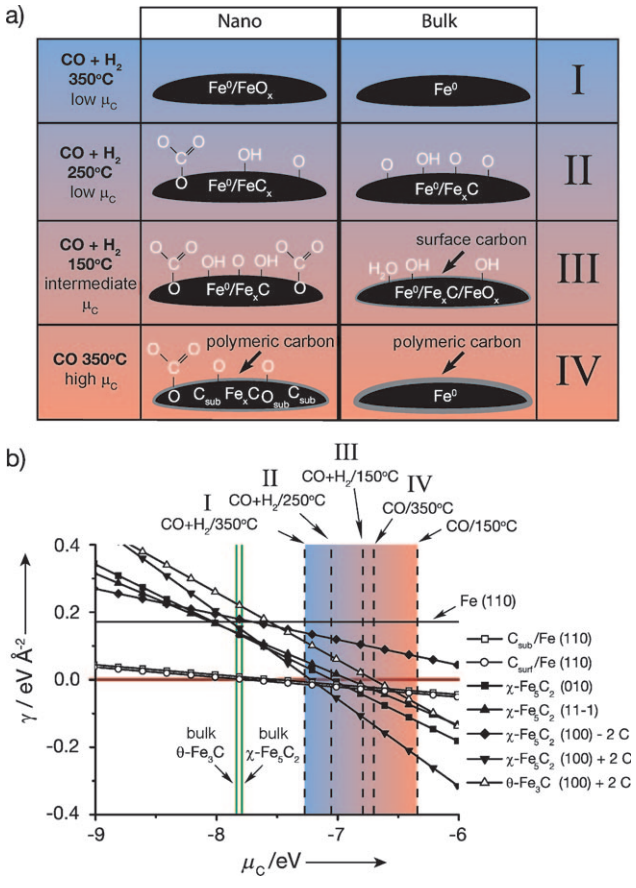


***Figure 4.*** a) Summary of Fe species and associated surface species during the different treatments of the two materials under study. b) Calculated thermodynamic stability of selected thin carbide layers and iron/carbon surfaces as a function of the chemical potential of carbon atoms, $\mu_C$. The shaded area and arrows indicate the experimental conditions applied in this study.

Figure 4b shows the stability of Fe (110) bound (sub)surface carbon and several modified carbide surface layers (layer thickness of five Fe layers) as a function of the chemical potential imposed by the gas-phase conditions. The surface free energy is given with respect to a bcc (body-centered cubic) Fe reference. Also indicated are the critical $\mu_C$ values at which bulk θ-$Fe_3C$ and χ-$Fe_5C_2$ carbides become stable. Phases with the lowest free surface energy are the most stable phases for given $\mu_C$. The conditions in our experiment (shaded area) were such that $\mu_C$ is in the stability range of surface and subsurface carbon and iron carbides. Thermodynamically, under our experimental conditions, both bulk θ-$Fe_3C$ and χ-$Fe_5C_2$ carbides are stable. However, at 350 °C in $CO/H_2$, it was observed that kinetically these bulk carbide phases could not form, possibly due to the competition with surface hydrogenation reactions. At these conditions, $\mu_C$ is also not low enough to induce the formation of a surface carbide layer, as bulk bcc Fe and surface/subsurface carbon are more stable. However, the latter species were not observed and might also be reacted away in the presence of $H_2$. At lower temperatures, the $\mu_C$ imposed by the gas-phase reservoir is in the range where the carbon covered χ-$Fe_5C_2$(100) surface carbide layer becomes thermodynamically more stable compared to surface and subsurface carbon and there is competition between the formation of the carbide phase and the hydrogenation of carbon atoms at the surface. Upon lowering the temperature, the formation of carbide surfaces becomes more favorable thermodynamically (Figure 4b). The formation of a bulk carbide phase might be inhibited under the low-temperature conditions, due to diffusion limitations and limited CO dissociation, therefore stabilizing a thin carbide surface layer.

During the CO treatment at 150 °C, $\mu_C$ is high. However, in the absence of $H_2$ and at low temperature, dissociated carbon on the surface of the catalyst is not hydrogenated away and not absorbed into the bulk as a result of slow kinetics. Some surface carbon is observed to form on the materials. It is noted here, however, that in our experiment the carbide formation might be hindered below 200 °C because of the oxidized state of the sample and the presence of surface carbonates in the bulk and nanoparticulate sample, respectively. Upon increasing the reaction temperature in CO, $\mu_C$ decreases again and the carbide phases become thermodynamically less and less favorable. Nonetheless, in the absence of $H_2$, $\mu_C$ is still higher at 350 °C as compared to the $CO/H_2$ conditions and there is no competition between the surface hydrogenation reaction and bulk carburization. Therefore, there is thermodynamic competition between the formation of bulk/surface carbides, and surface and subsurface carbon and the materials start forming surface carbon deposits. Temperatures above 300 °C might lead to thermal decomposition of the bulk χ-$Fe_5C_2$ carbide structure into θ-$Fe_3C$.[21] Our calculations show (Figure 4b) that even the most stable θ-$Fe_3C$ surface under these conditions, the carbon-covered θ-$Fe_3C$ (100) surface layer, cannot thermodynamically compete with surface and subsurface carbon species.

  

Our work illustrates the dynamic nature of the iron, oxygen, and carbon surface chemistry of nanoparticulate iron oxide in reactive gas atmospheres. It was shown that in this system there is competition between the formation of surface, subsurface, and carbide carbon species, whereas a bulk iron oxide reacted less dynamically and was susceptible to oxidation and surface carbon deposition. The results constitute a direct demonstration of the size dependency of iron oxide surface chemistry, while the application of ab initio atomistic thermodynamics accommodated the rationalization of the observed surface chemistry in both materials as a function a wide variety of experimental conditions.

Received: August 24, 2010
Revised: October 9, 2010
Published online: January 7, 2011

**Keywords:** heterogeneous catalysis · in situ spectroscopy · iron oxide · surface chemistry · X-ray photoelectron spectroscopy

[1] E. Roduner, *Nanoscopic Materials*, Royal Society of Chemistry, Cambridge, **2006**.
[2] A. Navrotsky, L. Mazeina, J. Majzlan, *Science* **2008**, *319*, 1635 – 1638.
[3] M. Mavrikakis, P. Stoltze, J. K. Nørskov, *Catal. Lett.* **2000**, *64*, 101 – 106.
[4] O. M. Wilson, M. R. Knecht, J. C. Garcia-Martinez, R. M. Crooks, *J. Am. Chem. Soc.* **2006**, *128*, 4510 – 4511.
[5] J. P. den Breejen, P. B. Radstake, G. L. Bezemer, J. H. Bitter, V. Frøseth, A. Holmen, K. P. de Jong, *J. Am. Chem. Soc.* **2009**, *131*, 7197 – 7203.
[6] H. Bluhm, M. Hävecker, A. Knop-Gericke, E. Kleimenov, R. Schlögl, D. Teschner, V. I. Bukhtiyarov, D. F. Ogletree, M. Salmeron, *J. Phys. Chem. B* **2004**, *108*, 14340 – 14347.
[7] F. Tao, M. E. Grass, Y. Zhang, D. R. Butcher, J. R. Renzas, Z. Liu, J. Y. Chung, B. S. Mun, M. Salmeron, G. A. Somorjai, *Science* **2008**, *322*, 932 – 934.
[8] D. Frank Ogletree, H. Bluhm, E. D. Hebenstreit, M. Salmeron, *Nucl. Instrum. Methods Phys. Res. Sect. A* **2009**, *601*, 151 – 160.
[9] A. Knop-Gericke, E. Kleimenov, M. Havecker, R. Blume, D. Teschner, S. Zafeiratos, R. Schlögl, V. I. Bukhtiyarov, V. V. Kaichev, I. P. Prosvirin, A. I. Nizovskii, H. Bluhm, A. Barinov, P. Dudin, M. Kiskinova in *Advances in Catalysis*, *Vol 52*, Elsevier, San Diego, **2009**, pp. 213 – 272.
[10] K. Reuter, M. Scheffler, *Phys. Rev. Lett.* **2003**, *90*, 046103.
[11] D. Teschner, Z. Révay, J. Borsodi, M. Hävecker, A. Knop-Gericke, R. Schlögl, D. Milroy, S. D. Jackson, D. Torres, P. Sautet, *Angew. Chem.* **2008**, *120*, 9414 – 9418; *Angew. Chem. Int. Ed.* **2008**, *47*, 9274 – 9278.
[12] P. Sautet, F. Cinquini, *ChemCatChem* **2010**, *2*, 636 – 639.
[13] M. E. Dry in *Catalysis – Science and Technology*, *Vol. 1* (Eds.: J. R. Anderson, M. Boudart), Springer, New York, **1981**, p. 159.
[14] E. de Smit, B. M. Weckhuysen, *Chem. Soc. Rev.* **2008**, *37*, 2758 – 2781.
[15] E. van Steen, M. Claeys, *Chem. Eng. Technol.* **2008**, *31*, 655 – 666.
[16] S. Vasudevan, M. S. Hegde, C. N. R. Rao, *J. Solid State Chem.* **1979**, *29*, 253 – 257.
[17] J. Haber, J. Stoch, L. Ungier, *J. Electron Spectrosc. Relat. Phenom.* **1976**, *9*, 459 – 467.
[18] C. S. Kuivila, P. C. Stair, J. B. Butt, *J. Catal.* **1989**, *118*, 299 – 311.
[19] X. Deng, A. Verdaguer, T. Herranz, C. Weis, H. Bluhm, M. Salmeron, *Langmuir* **2008**, *24*, 9474 – 9478.
[20] D. Teschner, A. Pestryakov, E. Kleimenov, M. Hävecker, H. Bluhm, H. Sauer, A. Knop-Gericke, R. Schlögl, *J. Catal.* **2005**, *230*, 186 – 194.
[21] S. Nagakura, *J. Phys. Soc. Jpn.* **1959**, *14*, 186.

  